Radio Jet Feedback on the Inner Disk of Virgo Spiral Galaxy Messier 58

Patrick M. Ogle[1] , Iván E. López[2,3,4] , Victoria Reynaldi[4,5] , Aditya Togi[6] , R. Michael Rich[7] , Javier Román[8,9,10] ,
Osmin Caceres[7], Zhuofu (Chester) Li[7,11] , Grant Donnelly[12] , J. D. T. Smith[12] , Philip N. Appleton[13] , and
Lauranne Lanz[14]

[1] Space Telescope Science Institute, 3700 San Martin Dr., Baltimore, MD 21218, USA
[2] Dipartimento di Fisica e Astronomia "Augusto Righi," Universitá di Bologna, via Gobetti 93/2, I-40129 Bologna, Italy
[3] INAF—Osservatorio di Astrofisica e Scienza dello Spazio di Bologna, via Gobetti 93/3, I-40129 Bologna, Italy
[4] Facultad de Cs. Astronómicas y Geofísicas, Universidad Nacional de La Plata, La Plata, Argentina
[5] Instituto de Astrofísica de la Plata (CONICET—UNLP), Paseo del Bosque s/n, 1900, La Plata, Argentina
[6] Department of Physics, 601 University Dr., Texas State University, San Marcos, TX 78666, USA
[7] Department of Physics and Astronomy, University of California, Los Angeles, CA, USA
[8] Kapteyn Astronomical Institute, University of Groningen, The Netherlands
[9] Instituto de Astrofísica de Canarias, Tenerife, Spain
[10] Departamento de Astrofísica, Universidad de La Laguna, Tenerife, Spain
[11] Department of Astronomy, University of Washington, Seattle, WA, USA
[12] Ritter Astrophysical Research Center, University of Toledo, OH, USA
[13] IPAC, California Institute of Technology, Pasadena, CA, USA
[14] The College of New Jersey, Ewing, NJ, USA

Abstract

Spitzer spectral maps reveal a disk of highly luminous, warm (>150 K) H_2 in the center of the massive spiral galaxy Messier 58, which hosts a radio-loud active galactic nucleus (AGN). The inner 2.6 kpc of the galaxy appears to be overrun by shocks from the radio jet cocoon. Gemini NIRI imaging of the H_2 1–0 S(1) emission line, Atacama Large Millimeter/submillimeter Array CO 2–1, and Hubble Space Telescope multiband imagery indicate that much of the molecular gas is shocked in situ, corresponding to lanes of dusty molecular gas that spiral toward the galactic nucleus. The CO 2–1 and ionized gas kinematics are highly disturbed, with velocity dispersion up to 300 km s^{-1}. Dissipation of the associated kinetic energy and turbulence, likely injected into the interstellar medium by radio-jet-driven outflows, may power the observed molecular and ionized gas emission from the inner disk. The polycyclic aromatic hydrocarbon (PAH) fraction and composition in the inner disk appear to be normal, in spite of the jet and AGN activity. The PAH ratios are consistent with excitation by the interstellar radiation field from old stars in the bulge, with no contribution from star formation. The phenomenon of jet-shocked H_2 may substantially reduce star formation and help to regulate the stellar mass of the inner disk and supermassive black hole in this otherwise normal spiral galaxy. Similarly strong H_2 emission is found at the centers of several nearby spiral and lenticular galaxies with massive bulges and radio-loud AGNs.

Unified Astronomy Thesaurus concepts: Active galaxies (17); Radio jets (1347); Shocks (2086)

1. Introduction

Low-power radio jets are ubiquitous in galaxies that host AGNs (Ho & Ulvestad 2001; Chiaraluce et al. 2019). While not as spectacular as those of their radio-galaxy and quasar cousins, these jets may have a significant impact on their host galaxies and also provide a testing ground for theories of AGN kinetic (radio jet) feedback. AGN feedback may limit star formation in galaxies by heating the interstellar medium (ISM) and intergalactic medium (IGM) or ejecting the ISM via outflows (Springel et al. 2005; Croton et al. 2006). While quasar feedback is thought to be crucial in halting star formation in the aftermath of transformative galaxy collisions, feedback by less luminous AGNs may also be important in regulating the gas content and star formation in the bulges and inner disks of normal spiral galaxies. In particular, low-power jets can push away dust, inflate radio bubbles and even accelerate ionized gas away from the center (e.g., Harrison et al. 2015).

Scaling relations between supermassive black holes (BHs) and their host galaxies, like the BH–bulge mass relation, imply a coevolution between them (Kormendy & Ho 2013). The cosmic star formation rate (SFR) density peaked at $z \sim 2$–3 (Madau & Dickinson 2014) and has declined since then, following a similar decrease in the cold gas density that fuels star formation (Boogaard et al. 2023). The BH accretion rate density, estimated from the quasar luminosity function, also peaks at $z \sim 2$–3 and then drops by more than an order of magnitude at $z < 1$ (Hopkins et al. 2006). The tight correlation between SFR and BH accretion rate across cosmic time (e.g., Aird et al. 2015; Yang et al. 2018) suggests that BH growth is closely linked to the star formation history of its host galaxy. At late times, radio jet feedback may serve to preserve these scaling relations in the presence of ongoing gas accretion.

H_2 emission is an excellent tracer of AGN feedback on molecular gas in active galaxies over a wide range of power, including starbursts, LINERs, Seyferts, quasars, and radio galaxies (Higdon et al. 2006; Veilleux et al. 2009; Ogle et al. 2010; Lambrides et al. 2019). AGNs in the Spitzer Infrared Nearby Galaxies Survey (SINGS; Kennicutt et al. 2003) show elevated H_2 emission compared to normal, star-forming galaxies (Higdon et al. 2006).
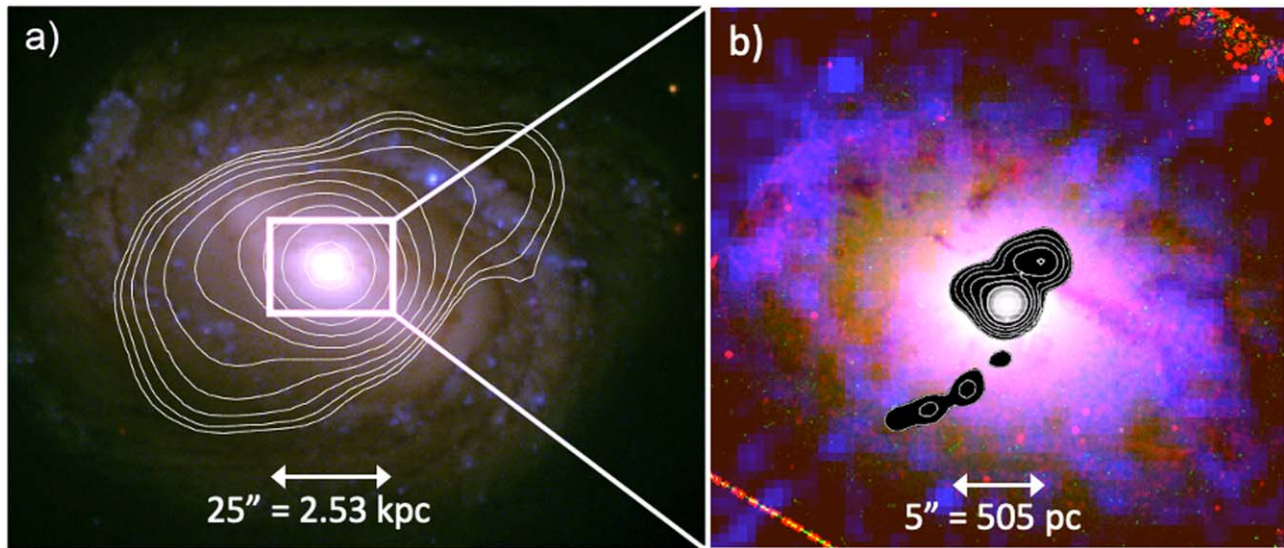
Figure 1. Archival multiwavelength observations of M58 with a close-up of the kiloparsec-scale disk. (a) SDSS u, g, r (blue, green, red) image with 4.9 GHz surface brightness contours of the radio jet from the VLA D array. (b) HST Hα (red) and F547M continuum (green), Chandra 0.5–8 keV X-rays (blue), and radio contours from the VLA at 1.4 GHz (A array). The blue, diagonal streak is an artifact of the Chandra readout. Both images are roughly centered on the AGN (R. A. = 189°43134, decl. = 11°81819), with standard orientation.

A spectacular case of low-power radio jet feedback is found in the nearby spiral galaxy NGC 4258, which hosts a LINER nucleus and low-power radio jet. In this galaxy, strong H$_2$ emission arises along the so-called anomalous arms, where molecular gas is shock-heated by a radio jet directed along the disk plane, driving ionized outflows (van der Kruit et al. 1972; Ogle et al. 2014; Appleton et al. 2018). The bulk heating of molecular gas to temperatures >200 K may directly suppress star formation in the inner disk of this spiral galaxy. Here, we report similarly spectacular radio jet feedback in the nearby spiral galaxy M58.

M58 (NGC 4579) resides in the Virgo Cluster at $z = 0.00506$. It is a massive, star-forming galaxy, with a mass in stars of 1.5×10^{11} $M_\odot$ and a dust-corrected SFR of 0.9 $M_\odot$ yr^{-1} (de los Reyes & Kennicutt 2019a, 2019b). It hosts a low-luminosity Seyfert 1.9 or LINER AGN (Maiolino et al. 1997; Barth et al. 2001) with an X-ray luminosity of $L_{\rm X} = 10^{34.1}$ W and a BH mass of $M_{\rm BH} \sim 10^{7.8}$ $M_\odot$ (Merloni et al. 2003). The AGN spectral energy distribution (SED) lacks a big blue bump component and is consistent with an advection-dominated accretion flow (Nemmen et al. 2014). The Very Large Array (VLA) reveals a 14 kpc long radio jet (Figure 1(a)), with a 1.4 GHz radio power of 1.0×10^{23} W Hz^{-1} (Ho & Ulvestad 2001; Vollmer et al. 2013). VLA C-array observations resolve the jet on the 100 pc scale, where it appears to be roughly aligned with the rotation axis of the galaxy's inner disk (Figure 1(b)). Narrowband (Hα) imaging shows a bright, kiloparsec-scale disk of ionized gas, and Chandra shows X-ray emission from hot gas closely associated with it (Figure 1(b); Pogge 1989; Eracleous et al. 2002).

We report on previously unpublished Spitzer spectral mapping and new Gemini NIRI imaging of the inner disk of M58, focusing on the impact of the AGN and its radio jet on molecular and ionized gas and dust in the central few kiloparsecs of the galaxy. This is supported by archival Atacama Large Millimeter/submillimeter Array (ALMA) CO 2–1 observations, ground-based and Hubble Space Telescope (HST) multiband imaging, and optical spectroscopy. We find extensive emission from kinematically disturbed molecular and

ionized gas, likely powered by shocks and turbulence driven by the radio jet. On the other hand, the polycyclic aromatic hydrocarbon (PAH) fraction and ratios appear to be normal and unaffected by the jet.

We adopt the SN 1989M (type Ia) distance of 21 Mpc (Ruiz-Lapuente 1996) to compute sizes and luminosities. The corresponding spatial scale is 101 pc arcsec^{-1}.

2. Observations

2.1. Spitzer Spectral Maps

We observed M58 as part of a Spitzer Infrared Spectrograph (IRS) program to study the effects of AGNs on their host galaxies (PI Smith, J.D. Program 3471). M58 was mapped using slit-stepping with both the SL and LL low-resolution gratings. We utilize only the central 55″5 × 55″5 regions of the maps that were covered by both gratings. The simultaneous background, covering an off-galaxy location, was subtracted from the map. We constructed spectral cubes using CUBISM (Smith et al. 2007a). The SL cubes cover 5.2–14.3 μm, with a pixel scale of 1″85 pixel^{-1} and a resolving power of 60–127. The LL cubes cover 13.9–38.3 μm, with a pixel scale of 5″07 pixel^{-1} and a resolving power of 57–126.

We use a novel method to model and measure the strengths of mid-infrared (MIR) spectral features and derived quantities in the Spitzer IRS spectral cubes. First, we fit each individual spaxel using a combination of dust continuum, PAH feature, and emission line models, similar to those used by PAHFIT (Smith et al. 2007b), utilizing the Python package LMFIT for Levenberg–Marquardt least-squares fitting (Newville et al. 2023). Next, we use the best-fit spectral parameters for each spaxel to generate feature flux maps. Finally, we use line and feature ratios and equivalent widths to identify and extract spatial regions with distinct MIR spectra. We note that this is a less-biased, empirical way of identifying, grouping, and extracting like spaxels than the more common method of extracting spectra in circular or elliptical apertures. We let the data tell us which regions to extract, and spatially disjoint regions with similar spectra can be combined for the highest

possible spectral signal-to-noise ratio. We do not consider the instrumental point-spread function (PSF) when fitting the spectral cube. However, linking the fit parameters of associated spectral features (e.g., all PAH features or all H_2 lines) helps to mitigate spatial and spectral sampling issues at the initial spaxel-fitting stage, and combining multiple spaxels in the subsequent spectral extractions and model-fitting largely averages over any sub-PSF variations.

2.2. Gemini NIRI Imaging

Data were obtained using the Near Infrared Imager (NIRI) on the Gemini-North Telescope at Maunakea in Hawaii during semester 2021A (program GN2021A-Q-137, PI: I.E. Lopez) on nights with the best photometric quality (IQ20%). The observations were designed to map H_2 emission at high spatial resolution, resolving structures down to 35 pc. We used the narrowband filter G0216 to isolate the H_2 1–0 S(1) line centered at 2.12 μm and the K-continuum filter centered at 2.09 μm to obtain the continuum emission. The f/6 configuration was adopted, providing a field of view of $120\square''$, pixel size of $0.''117$, and median seeing FWHM of $0.''35$. We applied a dithering pattern to cover the gaps and remove the sky background, cosmic rays, and bad pixels. In each filter, we coadded sets of 8×30 s exposures to avoid saturation of the galaxy's center. In total, each filter has an exposure on-source of 2160 s. We corrected for thermal emission, dark current, and hot pixels using darks and flat frames. We also applied a flux calibration using images from both narrow filters of the standard star FS132. We used Gemini Observatory's software DRAGONS (Data Reduction for Astronomy from Gemini Observatory North and South) for the data reduction (Labrie et al. 2019).

2.3. Optical Narrowband Imaging

We observed M58 in Hα + [N II] with the f/3.2, 0.7 m Jeanne Rich Telescope (JRT; Rich et al. 2019) in order to image ionized gas across the galaxy to low surface brightness levels. The FLI09000 CCD camera has $2.''23$ pixels and a 0.57 deg^2 ($45' \times 45'$) field of view. We took $\sim 300 \times 5$ minute exposures (25 hr) in a custom 4 nm wide interference filter, centered at 660.5 nm; and $\sim 120 \times 5$ minute (10 hr) in a custom 20 nm wide offband continuum filter centered at 644 nm. The on-band filter was designed to cover the Hα emission line over a redshift range of $z = 0.0050$–0.0084 and also includes the adjacent [N II] emission lines. The observations were aggressively dithered to minimize background gradients and to allow building of the flat with the science images. The reduction was carried out with standard subtraction of averaged bias and dark images. The flat was constructed by masking the science images with SExtractor (Bertin & Arnouts 1996) and NoiseChisel (Akhlaghi & Ichikawa 2015), which, after normalization and combination, produces the flat. The astrometry was calculated using the Astrometry.net software package (Lang et al. 2010) and SCAMP (Bertin 2006). The images were photometrically calibrated to the Sloan Digital Sky Survey (SDSS) and sky-subtracted with a conservative procedure using Zernike polynomials, avoiding an oversubtraction of the images. Finally, all images were combined with a weighted mean. The emission line flux is calibrated against the flux measured inside an $r = 37''$ diameter by Theios et al. (2016): $F(H\alpha + [N II]) = 2.5 \times 10^{-15}$ W m^{-2}.

2.4. Optical Spectroscopy

We observed M58 with the Kast Double Spectrograph on the 3 m Shane Telescope at Lick observatory on 2022 May 26. We used the 600/4310 grating to cover a wavelength range of 3500–5600 Å on the blue side and the 1200/5000 grating to cover 5760–6790 Å on the red side. We used a $2.''0$ wide slit, giving a spectral resolution of $\sigma = 0.90$ (40 km s^{-1}) at 6600 Å. This long slit, with a length of $400''$, was oriented at a position angle (PA) = $57°$. The detector samples the spectrum at 1.02 Å pixel^{-1} on the blue side and 0.65 Å pixel^{-1} on the red side. We extracted spectra in 29 variable-sized spatial regions along the slit. Data reductions included bias subtraction, flat-fielding, cosmic-ray rejection, off-source background subtraction, wavelength calibration using an internal lamp spectrum, flux calibration with a standard star, and correction for wavelength-dependent atmospheric extinction. Given the variability of the sky background on a timescale of 10 minutes, primarily from artificial light pollution that changes with elevation, it was necessary to utilize a region along the slit that had the weakest source signal to make an additional background correction.

2.5. Archival Data

VLA 4.9 GHz (D array) and 1.4 GHz (A array) observations (Figure 1(a)) reveal a radio jet at arcsecond to arcminute scales (Ho & Ulvestad 2001; Vollmer et al. 2013). We utilize the PHANGS-ALMA v4.0 CO 2–1 data cube and moment maps for M58, from ALMA data set ADS/JAO.ALMA# 2017.1.00886.L: P.I. Schinnerer (large program) (Leroy et al. 2021a, 2021b). The maps have $1''$ angular resolution and ~ 2.5 km s^{-1} velocity resolution. We utilize photometry from the PACS instrument (Poglitsch et al. 2010) on the ESA Herschel Space Observatory[15] (Pilbratt et al. 2010) to measure the cold dust mass. Multiband HST imaging in the F791W, narrowband F658N, and offband F547M filters provides a high-resolution view of Hα and dust absorption (Figure 1(b)). Galaxy Evolution Explorer (GALEX) far-ultraviolet (FUV) imagery is utilized to trace recent star formation. Chandra ACIS-S imaging spectroscopy (Obs. ID 807; Eracleous et al. 2002) highlights emission from hot ($\sim 10^7$ K) gas at the galactic center (Figure 1(b)).

3. Results

The nucleus of M58 is bright in all MIR spectral components, including ionized gas, H_2, PAH features, and warm dust (Figure 2). Silicate emission at 9–13 μm from warm dust heated by the AGN is only detected in a central, unresolved point source, following the Spitzer PSF. The inner ($r = 2.6$ kpc) disk is traced by diffuse 11.3 μm PAH emission. The 7.7 μm PAH feature and the [Ne II] 12.8 μm line are enhanced in star-forming regions found in the spiral arm of the galaxy that passes through the NW corner of the maps.

The most striking feature in the Spitzer spectral maps (Figure 2) is the unusually luminous, extended H_2 pure rotational line emission in the inner disk. The Gemini NIRI image of the H_2 1–0 S(1) rovibrational line at 2.12 μm (Figure 3) has a very similar spatial distribution to the lower-

---

[15] Herschel is an ESA space observatory with science instruments provided by European-led Principal Investigator consortia and with important participation from NASA.
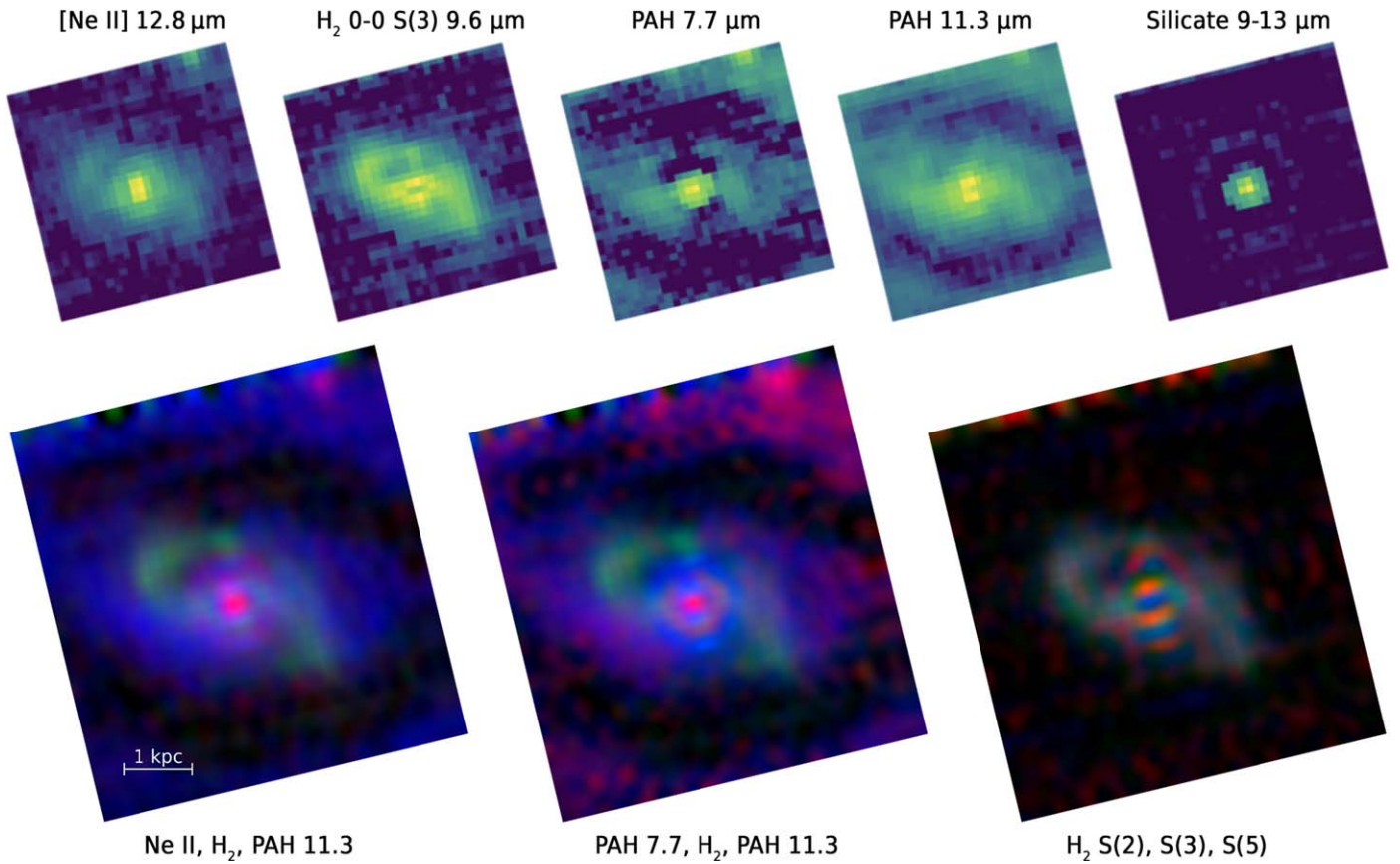
Figure 2. Spitzer spectral feature maps of M58, extracted from the IRS SL spectral data cube. Top: individual feature maps at native resolution, centered on the nucleus, and at the standard orientation. The silicate dust emission is localized to the unresolved AGN point source and follows the $\sim$9–13 μm PSF. Bottom: multicolor feature maps, covering the same area, but resampled to a finer grid using sinc interpolation. Bottom left: $r, g, b =$ [Ne II] 12.8 μm, H_2 S(3) 9.6 μm, PAH 11.3 μm. Both the AGN and a star-forming region in the NW spiral arm show up as red, neutral PAH emission from diffuse ISM blue, and shocked molecular gas green. Bottom center: $r =$ PAH 7.7 μm, $g = H_2$ S(3) 9.6 μm, $b =$ PAH 11.3 μm. Ionized PAH emission shows up as red, neutral PAH emission blue, and warm molecular gas green. Bottom right: $r, g, b = H_2$ S(2), S(3), S(5) pure rotational lines, following warm molecular gas over a range of temperatures. Note: the Airy rings of the AGN PSF, increasing in diameter with wavelength, are not real structures in the galaxy.

energy H_2 pure rotational lines and similar flux to the H_2 0–0 S(3) line (Table 1). The $\sim$10$\times$ higher resolution Gemini image clearly shows that the warm H_2 follows the dust lanes resolved by HST. There is a weaker association of H_2 with molecular gas traced by the ALMA CO 2–1 map (Figure 3; Leroy et al. 2021a).

There appear to be significant differences in the spatial distributions of warm H_2 rovibrational emission and CO 2–1. In particular, the H_2 emission is most intense closest to the nucleus and radio jet, while the CO 2–1 emission appears to peak along the spiral dust lanes just exterior to the nucleus, with additional clumps along the outer circumference of the inner disk. The H_2 emission shows similar clumping in the inner disk but lacks a detailed correspondence to the clumps in the CO 2–1 maps. The CO 2–1 lines most likely trace cooler, denser clumps than H_2 1–0 S(1), which are nonetheless also shock-heated, as revealed by their unusually high surface brightness compared to CO 2–1 in the outer spiral arms of the galaxy.

The [Ne II] 12.8 μm emission from ionized gas in the inner disk follows a similar pattern to that seen in H_2, suggesting that it is closely associated with the warm molecular gas and energized by the same source (Figure 2). Similarly, $H\alpha$ + [N II] correlates with H_2 in the dust lanes seen in the HST image (Figure 3). Additional diffuse ionized gas emission surrounds the nucleus and fills the inner disk.

4. Discussion

As described in Section 2.1, we fit the individual spaxels in the Spitzer spectral cube with a combination of dust continuum, PAH, and emission line features. Then we use the models to create feature flux maps for all model components (Figure 2). Next, we use the PAH 7.7/11.3 and H_2 S(3)/PAH 11.3 μm ratios measured from these maps to identify zones with distinct MIR spectra (Figure 4: SF Zone, inner disk Zones 1, 2, and 3, and NUC). These ratios indicate the relative contributions of star formation, diffuse ISM, and shocks to the MIR spectra. Spaxels in the SF Zone were selected to have PAH 7.7/11.3 $>$0.9, and those in inner disk Zones 1–3 PAH 7.7/11.3 $\leqslant$0.9. Zones 1–3 were further selected to have H_2 S(3)/PAH 11.3 in the ranges $<$0.25, 0.25–0.7, and $>$0.7, respectively. The nucleus was not identified by feature ratios. Instead, we sum the spectrum of the spatially unresolved nucleus (NUC) inside a 5×5 spaxel (934 pc $\times$ 934 pc) box centered on the AGN point source, covering the central peak of the PSF. We model the summed spectra of each zone, allowing all PAH feature fluxes to vary independently, and tabulate the feature fluxes of the best-fit models for the zones (Table 1).

4.1. PAH Ratios Unaffected by Jet Feedback

The PAH 7.7/11.3 ratio is primarily an indicator of PAH ionization level, set by the UV radiation field, and is typically
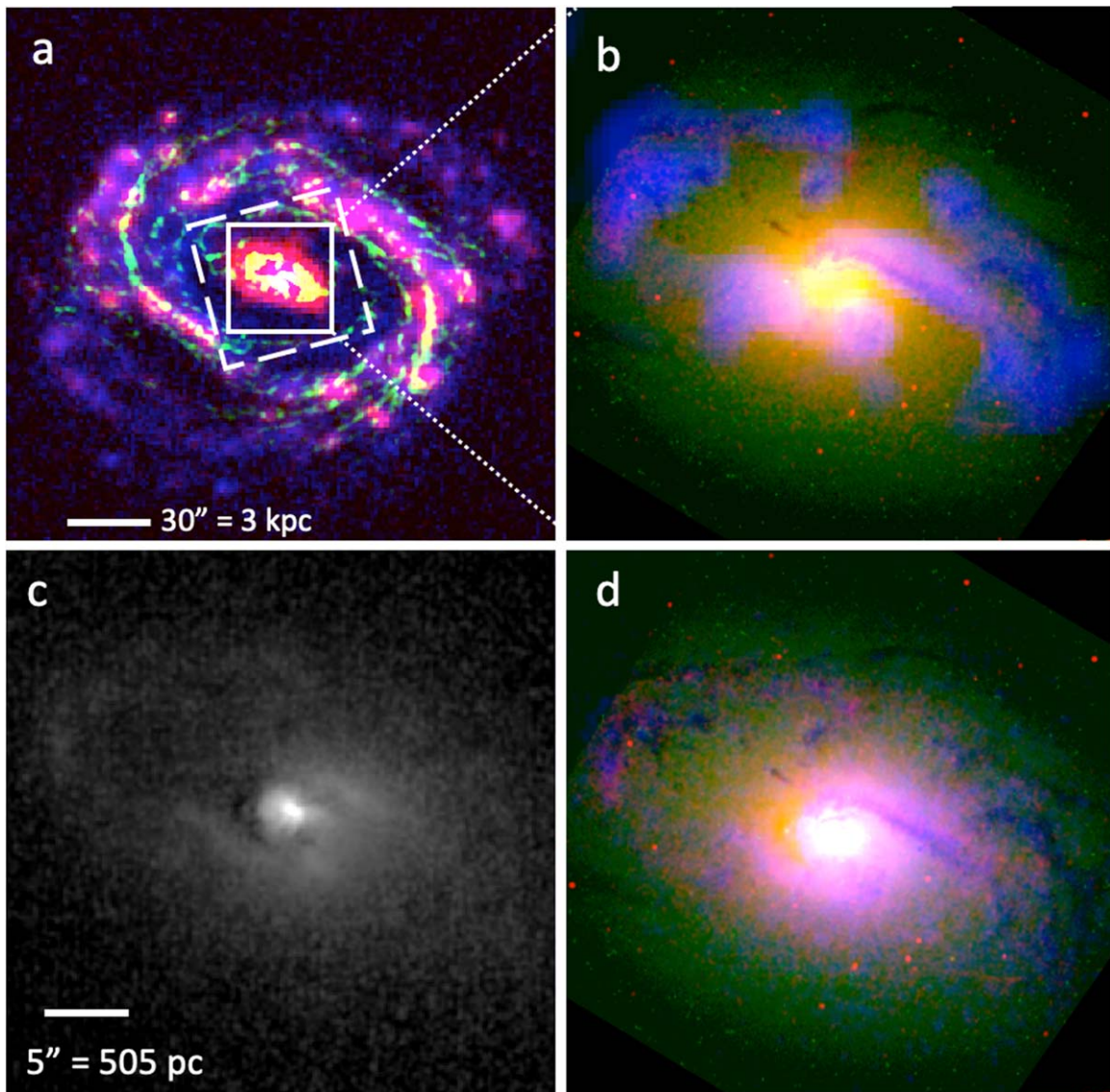
Figure 3. (a) Hα + [N II], CO 2–1, and GALEX FUV (*r, g, b*) image of M58. While the outer disk features star formation along the spiral arms, the inner disk is weak in FUV emission, but strong in Hα + [N II] emission from jet-shocked, ionized gas. The region mapped by Spitzer IRS is indicated by the long-dashed boundary. (b) HST Hα + [N II], F547M continuum, and CO 2–1 (*r, g, b*). Ionized gas emission peaks at the nucleus but also correlates with molecular gas in the dust lanes. (c) Gemini NIRI image of H_2 1–0 S(1), tracing shock-heated warm molecular gas. (d) HST Hα + [N II], F547M continuum, and H_2 1–0 S(1) (*r, g, b*) image of the inner disk of M58. There is a rough correspondence between the two warm molecular gas tracers, but the H_2 emission is relatively stronger in the nucleus and inner spiral. Clumpy H_2, CO, and ionized gas are found along the outer edge of the inner disk. Lower-surface-brightness ionized gas emission is found throughout the inner disk. All images are centered on the AGN, at standard orientation. Zoomed-in panels (b)–(d) are all at the same scale.

highest in photodissociation regions (PDRs) associated with regions of active star formation (Draine & Li 2007; Chastenet et al. 2023). Most of the SF Zone spaxels fall in the NW spiral arm at the corner of the map (Figure 4), where our Hα image shows an abundance of discrete star-forming H II regions (Figure 3(a)). We estimate the star formation rate using the prescription SFR(PAH 7.7) = $2.4 \times 10^{-9} M_\odot$ yr^{-1} L(PAH 7.7) / $L_\odot$ (Roussel et al. 2001). The mean SFR surface density in the SF Zone is $\Sigma_{SFR} = 5.7 \times 10^{-3} M_\odot$ yr^{-1} kpc^{-2}, roughly twice the mean for the whole galaxy (de los Reyes & Kennicutt 2019a, 2019b).

In comparison, there is relatively little star formation in Zones 1–3 of the inner disk, which display low PAH 7.7/11.3 ratios. The PAH 6.2/11.3 and PAH 8.6/11.3 ratios, which track ionization, are also low in the inner disk compared to the SF Zone (Table 1). The bright ionized gas emission in this region has emission line ratios characteristic of shocks or LINER photoionization rather than star formation (Section 4.7). Furthermore, the FUV continuum surface brightness of the inner disk is low (Figure 3(a)) and there are no obvious clumps in the HST Hα + [N II] image attributable to star formation (Figure 3(d)). We estimate SFR(PAH 7.7) < 0.03 $M_\odot$ yr^{-1} and a mean SFR surface density of $<3 \times 10^{-3} M_\odot$ yr^{-1} kpc^{-2} in Zones 1–3 combined. On the other hand, an ultracompact nuclear ring of young stars with a radius of 150 pc is seen at near-UV (NUV) wavelengths by HST (Comerón et al. 2008). The elevated UV field in this ring may account for the slightly elevated PAH 7.7/11.3 ratio in the nucleus (1.1) compared to the inner disk (0.6–0.7).

Low-luminosity AGNs are often found in the bulges of massive galaxies where there is little star formation activity, and their radio luminosity correlates with bulge mass (Nagar

Table 1
M58 Line and Feature Fluxes

Feature	SF Zone	Disk Zone 1	Zone 2	Zone 3	Nucleus
PAH 6.2 [1.0×10^{-17} W m^{-2}]	16.4 (1.1)	17.0 (1.9)	18.1 (3.0)	2.5 (0.9)	15.0 (3.3)
PAH 7.7	49.6 (3.2)	35.4 (5.4)	39.0 (8.8)	6.0 (1.0)	51.8 (4.7)
PAH 8.6	11.8 (0.7)	7.8 (1.2)	...	...	...
PAH 11.3	24.8 (1.3)	47.9 (2.2)	61.7 (3.4)	8.8 (1.2)	47.2 (4.4)
PAH 12.0	6.4 (0.8)	12.4 (1.4)	17.5 (2.2)	2.7 (0.7)	6.0 (2.7)
PAH 12.6	13.7 (0.7)	22.9 (1.2)	29.2 (1.8)	...	17.2 (2.0)
PAH 17	10.2 (2.0)	20.6 (5.7)	28.8 (7.3)	5.8 (1.3)	19.0 (4.4)
PAH 6.2/11.3 [flux ratio]	0.66 (0.05)	0.36 (0.04)	0.29 (0.05)	0.28 (0.11)	0.32 (0.08)
PAH 7.7/11.3	2.00 (0.17)	0.74 (0.12)	0.63 (0.15)	0.69 (0.14)	1.10 (0.14)
PAH 8.6/11.3	0.48 (0.04)	0.16 (0.03)	...	...	...
PAH 12.0/11.3	0.26 (0.03)	0.26 (0.03)	0.28 (0.04)	0.31 (0.09)	0.13 (0.06)
PAH 12.6/11.3	0.55 (0.04)	0.48 (0.03)	0.47 (0.04)	...	0.36 (0.05)
PAH 17/11.3	0.41 (0.08)	0.43 (0.12)	0.47 (0.12)	0.66 (0.17)	0.40 (0.10)
H$_2$ 0–0 S(5) 6.91 [1.0×10^{-17} W m^{-2}]	0.92 (0.34)	2.21 (0.60)	12.62 (0.94)	3.46 (0.32)	10.09 (1.49)
H$_2$ 0–0 S(4) 8.03	0.35 (0.29)	...	5.17 (0.96)	1.41 (0.28)	3.38 (0.62)
H$_2$ 0–0 S(3) 9.66	0.85 (0.16)	6.05 (0.33)	22.85 (0.57)	7.07 (0.19)	14.62 (0.73)
H$_2$ 0–0 S(2) 12.28	0.53 (0.19)	2.19 (0.32)	8.29 (0.51)	2.64 (0.18)	4.37 (0.59)
H$_2$ 0–0 S(1) 17.04	1.38 (0.33)	9.06 (0.54)	14.77 (0.70)	3.54 (0.18)	9.35 (1.80)
H$_2$ 0–0 S(0) 28.22	0.33 (0.07)	0.81 (0.16)	0.70 (0.20)	0.14 (0.07)	0.66 (0.33)
H$_2$ 0–0 S(1)/H$_2$ 0–0 S(0) [flux ratio]	4.2 (0.3)	11.2 (0.2)	21.1 (0.3)	25.3 (0.5)	14.2 (0.5)
H$_2$ S(3)/PAH 11.3	0.034 (0.007)	0.13 (0.01)	0.37 (0.02)	0.80 (0.11)	0.31 (0.03)
H$_2$ 1–0 S(1) [1.0×10^{-17} W m^{-2}]	...	...	33.1 (1.0)	6.70 (0.20)	19.4 (0.58)
Hα + [N II] [1.0×10^{-17} W m^{-2}]	9.26 (0.09)	22.45 (0.02)	76.34 (0.08)	20.82 (0.02)	97.07 (0.10)
Solid angle [□″]	281	541	318	92	86
T_l [K]	50	150 (20)	240 (20)	300 (20)	160 (60)
n [power-law index]	4.8 (0.2)	5.3 (0.2)	4.9 (0.2)	5.4 (0.3)	4.3 (0.3)
M(warm H$_2$) [$M_\odot$]	3.4×10^7	5.4×10^6	2.2×10^6	3.7×10^5	3.0×10^6
M_{dust} [$M_\odot$]	4.5×10^5	1.3×10^6	1.7×10^6	...	2.8×10^5
M(warm H$_2$)/M_{dust}	76	4.2	1.3	...	11
F(CO 2–1) [Jy km s^{-1}]	48	76	286	119	194
L'(CO 2–1) [K km s^{-1} pc^2]	1.3×10^7	2.0×10^7	7.7×10^7	3.2×10^7	5.2×10^7
M_{gas}(CO 2–1) [$M_\odot$]	5.2×10^7	8.2×10^7	3.1×10^8	1.3×10^8	2.1×10^8
M_{gas}(CO 2–1)/M_{dust}	115	63	182	...	750
L(H$_2$ S(0)–S(3)) [10^{33} W]	0.16 (0.02)	0.96 (0.04)	2.46 (0.06)	0.71 (0.02)	1.53 (0.07)
L(Hα + [N II]) [10^{33} W]	0.489 (0.005)	1.185 (0.001)	4.029 (0.004)	1.099 (0.001)	5.123 (0.005)
L(CO 2–1) [10^{30} W]	2.0	3.1	11.6	4.8	7.8
L(2–10 keV) [10^{33} W]	...	...	...	...	20

et al. 2005). Star formation may be suppressed in such an environment by radio jet feedback, morphological quenching (Martig et al. 2009), or the increased velocity dispersion of gas in the gravitational field of the bulge (Gensior et al. 2020). The PAH 7.7/11.3 ratios of 0.6–0.7 observed in Zones 1–3 are comparable to those found for dusty elliptical galaxies that lack star formation (Kaneda et al. 2008). The PAH emission from the inner disk of M58 (and elliptical galaxies) is most likely excited by the interstellar radiation field from old stars in the galactic bulge, as demonstrated for dust continuum emission in the bulge of M31 (Groves et al. 2012).

It has been suggested that AGN X-rays or shocks may destroy small PAH molecules and thereby lower the PAH 7.7/ 11.3 ratio in galaxies with AGN activity (Smith et al. 2007a; Diamond-Stanic & Rieke 2010; García-Bernete et al. 2022; Zhang et al. 2022). However, it is difficult to disentangle the effects of PAH size distribution and UV ionization level on the PAH 7.7/11.3 ratio (Draine et al. 2021). Notably, there is no significant variation in the PAH 7.7/11.3 ratio or other PAH ratios across Zones 1–3, in spite of their differences in H$_2$ surface brightness and H$_2$/PAH 11.3 ratio. This may indicate that the PAH composition is insensitive to the relatively weak shocks from the low-power radio jet that are heating the H$_2$.

There is a strong correlation between the intensities of the PAH 17 μm and PAH 11.3 μm features in SINGS galaxies, as both arise from neutral PAHs. (Smith et al. 2007a). There is an indication that the PAH 17/11.3 μm ratio may be enhanced in both SINGS galaxies and ellipticals with low-luminosity AGNs, compared to galaxies without an AGN (Kaneda et al. 2008). However, we find normal levels of PAH 17 emission in all regions of M58, with PAH 17/11.3 = 0.4–0.7, compared to 0.35–0.72 for the SINGS sample and 0.08–1.5 for ellipticals. The PAH 17/11.3 ratio is the same in the inner disk and SF Zone. The relatively large uncertainty in the PAH 17 μm measurement for the nucleus precludes a definitive statement on whether or not it is enhanced.

4.2. Shock-heated Molecular Gas

We present H$_2$ fluxes in Table 1. We expect the H$_2$ 0–0 S(3)/PAH 11.3 ratio to roughly follow the ratio of warm (> 150 K) H$_2$ to total gas mass, assuming that the PAH 11.3 carrier abundance is constant, which may hold true in the absence of significant variations in metallicity and ionization. The alternative H$_2$ 0–0 S(0–3)/PAH 7.7 ratio has been used as a shock indicator in radio galaxies (Ogle et al. 2010), but has the disadvantages of (1) being affected by photoionization in
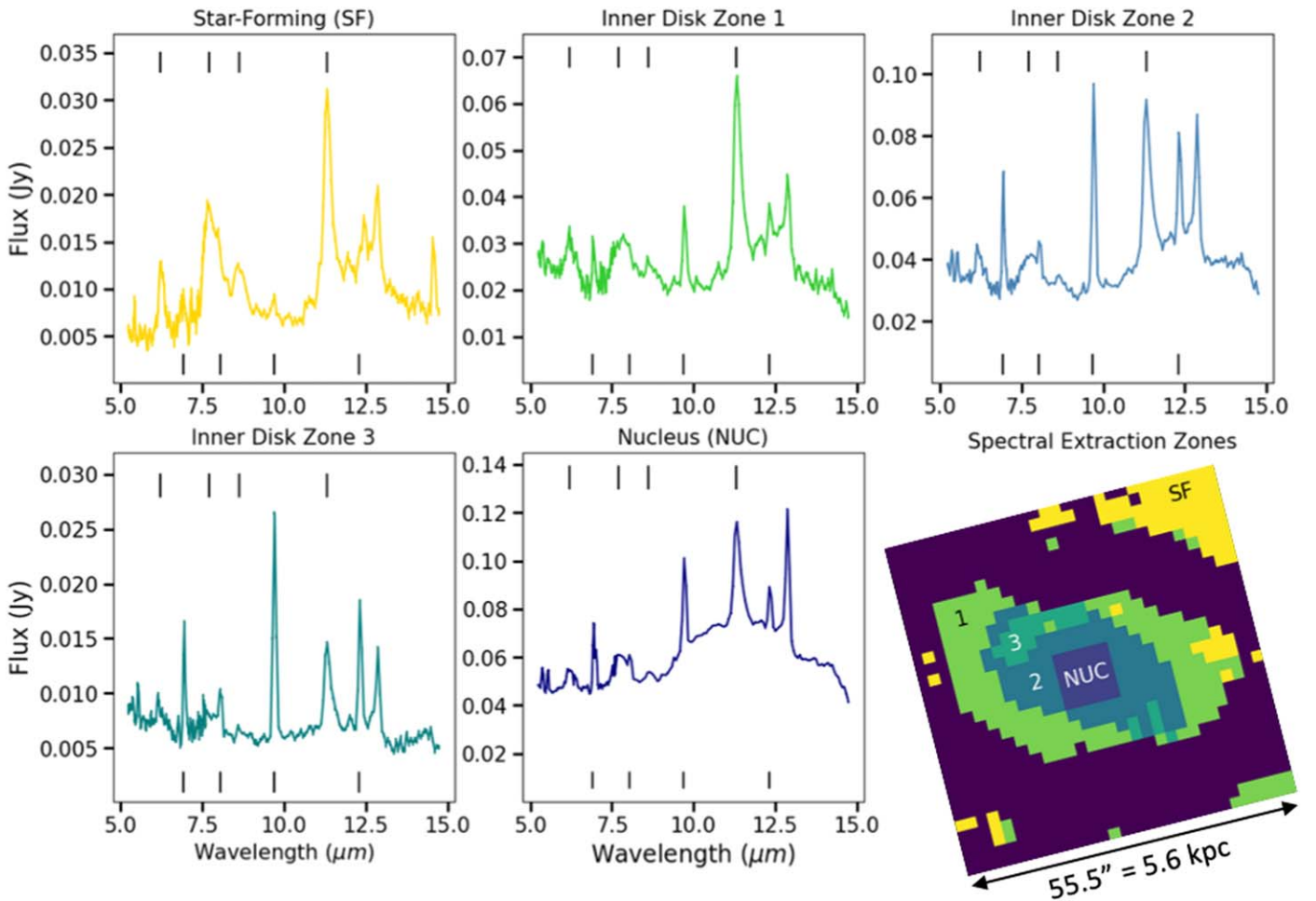
Figure 4. Spitzer IRS spectra of M58 regions selected by PAH 7.7/11.3 μm and H_2 S(3)/PAH 11.3 μm feature ratios. A color-coded map of spaxels included in each spectral extraction zone is given at bottom right, at standard orientation. PAH feature wavelengths (6.2, 7.7, 8.6, 11.3 μm) are indicated by vertical marks at the top of each panel, and H_2 0–0 pure rotational lines at the bottom (S(5), S(4), S(3), S(2)). The PAH 7.7/11.3 ratio is high in the SF Zone and low in the other zones where star formation is absent. The H_2 S(3)/PAH 11.3 μm ratio, highest in Zone 3, reflects the fraction of shock-heated molecular gas.

PDRs, (2) the weakness of PAH 7.7 emission in a low UV field, and (3) requiring measurement of four H_2 lines. We recommend using H_2 0–0 S(3)/PAH 11.3 instead, which is less sensitive to PAH ionization and only requires the measurement of two adjacent spectral features.

We find a low H_2 S(3)/PAH 11.3 ratio of 0.034 ± 0.007 in the SF Zone, consistent with PDR emission. The ratio is much greater in the inner disk, ranging from 0.13 at its outer edge (Zone 1) to its greatest value of 0.80 in Zone 3. Its value in the nucleus is also high (0.31 ± 0.03). We suggest that shocks and turbulence driven by the radio jet cocoon or jet-driven outflows may be responsible for the very luminous, extended H_2 emission that we observe in the inner disk of M58.

We fit the H_2 excitation diagram for each spectral zone with a power-law temperature distribution $dN/dT \sim T^{-n}$ (Figure 5; Table 1), following the method of Togi & Smith (2016). A continuous temperature distribution is expected for molecular gas with a range of densities, and a power-law distribution provides a good fit to the data. This is preferable to two-temperature models, which arbitrarily split the temperature distribution into two bins. The power-law model is parameterized by the power-law index n, the minimum detectable H_2 temperature T_l, and the total mass of warm H_2. It is clear from the excitation diagrams (Figure 5) and H_2 0–0 S(1)/H_2 0–0 S(0) ratios (Table 1) that the SF region has relatively more H_2

at lower temperature than do the inner disk and nucleus. Our best-fit temperature distribution models have $n = 4.32$–5.44, similar to values for the SINGS galaxy sample, which have a mean value of $n = 4.84 \pm 0.61$ (Togi & Smith 2016). For constant T_l, smaller values of n indicate relatively more molecular gas at high temperatures. For constant n, larger values of T_l indicate relatively more warm gas contributing to the H_2 emission lines. We find that n is fairly constant in the inner disk, but that T_l increases from 150 K in Zone 1 to 300 K in Zone 3, following the trend of increasing H_2 surface brightness and H_2/PAH 11.3 ratio. The nucleus, on the other hand, has lower T_l than Zone 3 and Zone 2, consistent with its lower H_2/PAH 11.3 ratio. The SF region has T_l pegged at a value of 50 K, below which the H_2 lines are not effectively emitted.

The total warm H_2 mass in the inner disk and nucleus is $1.1 \times 10^7 \ M_\odot$. In comparison, the total H_2 mass within $r = 2.1$ kpc, estimated from the CO 1–0 flux, is $\sim$50 times greater, at $5 \times 10^8 \ M_\odot$ (García-Burillo et al. 2009). Similarly, we estimate a cold molecular mass of $5.2 \times 10^8 \ M_\odot$ from the ALMA CO 2–1 flux in the same region, assuming the standard $\alpha_{CO} = 4 \ M_\odot/(K \ km \ s^{-1} \ pc^2)$ and $R_{21} = 0.6$. However, the CO mass estimates are sensitive to the distribution of molecular gas temperature. In the shocked inner disk of M58, both lines are enhanced at the elevated temperatures that we measure for
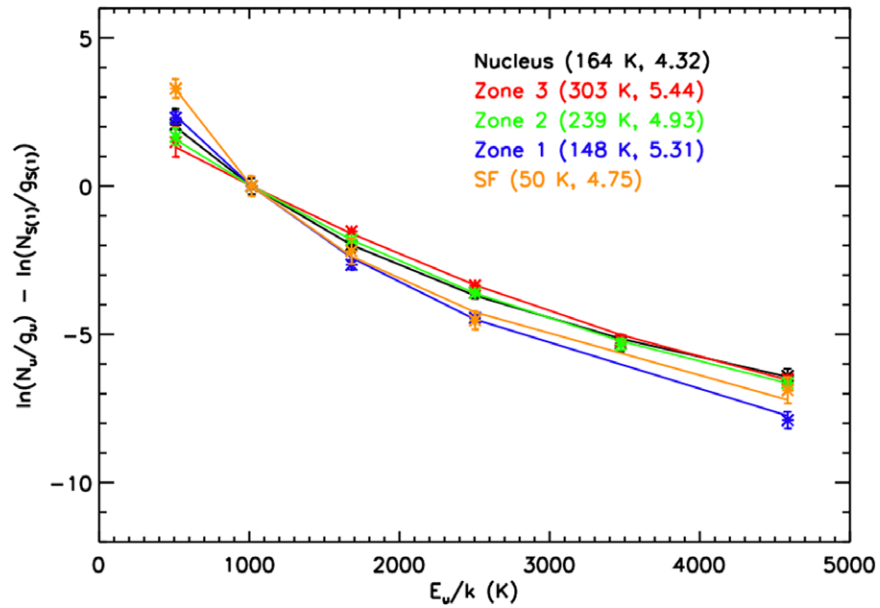
Figure 5. H_2 excitation diagrams for each zone, including pure rotational line levels S(0) through S(5). Column densities (data points) are normalized to the H_2 0–0 S(1) upper level, for purposes of comparison. Power-law model fits to the temperature distribution of each zone are indicated by the solid lines, with fit parameters (T_l, n) given in parentheses (see also Table 1). The SF region has the highest H_2 0–0 S(0) upper level column density, consistent with a relatively cooler temperature distribution.

warm H_2, leading to an overestimate of the cold molecular gas mass.

4.3. Dust Mass and PAH Abundance

In order to estimate the dust mass in each zone, we measured photometry from GALEX FUV and NUV, SDSS *ugriz*, our Gemini *Ks* image, Spitzer IRAC bands 1–4, PAH 7.7, 11.3 μm, MIPS 24 μm, and Herschel PACS 70, 100, and 160 μm bands (Figure 6). We fit each SED with a grid of CIGALE models (Boquien et al. 2019; Nersesian et al. 2019; Yang et al. 2020), using a Chabrier initial stellar mass function with solar metallicity and delayed star formation history for the stellar population, modified by dust extinction. We use the dust emission models of Draine et al. (2014), with dust grain densities reduced by a factor of 0.81 compared to Draine & Li (2007). We turned off the nebular emission, which would otherwise require shock modeling. The best-fit dust model has a PAH mass fraction $q_{PAH} = 0.019 \pm 0.003$, apparently lower than that of the diffuse ISM in the solar neighborhood ($q_{PAH} = 0.045$). However, CIGALE does not self-consistently account for the SED incident on the PAH molecules. Draine et al. (2014) find that a similar value of $q_{PAH} = 0.02$ in the central 1 kpc of M31 corrects to 0.04–0.05 after properly accounting for the SED of the bulge stars. Assuming a similar correction applies at the center of M58, the actual q_{PAH} appears to be consistent with the Galactic ISM and M31, with no indication of PAH depletion.

The dust masses derived from our SED fits of each zone are given in Table 1 (except Zone 3, which is too small to resolve at long wavelengths). We find a total dust mass of $M_{dust} = 3 \times 10^6$ $M_\odot$ from our fit of the combined SED of Zones 1–3, excluding the nucleus. Assuming a standard dust mass percentage of 1%, this corresponds to a total gas mass of 3×10^8 $M_\odot$. The molecular gas mass estimated above from CO 1–0 and 2–1 is a factor of 1.8 greater than this, confirming that these CO emission lines are boosted by shocks throughout the

inner disk. In the nucleus, the CO 2–1 line is boosted by a factor of $\sim$8 relative to dust emission, indicating even more heating of molecular gas by the jet. Using the lower gas mass estimated from dust and assuming that most of the gas in the inner disk is molecular yields warm H_2 percentages of 1%–4% in Zones 1 and 2. On the other hand, Zone 1 and the SF Zone have $M(CO\ 2–1)/M_{dust}$ values that are consistent with the Galatic value of $\sim$100, indicating that the CO emission is not boosted in the outer part of the inner disk. Evidence for jet shock-heated CO is found under similar conditions in NGC 4258, where the standard α_{CO} value yields an estimate of molecular gas mass that is $\sim$10$\times$ greater than that inferred from the dust mass estimated from SED fitting (Ogle et al. 2014).

It is also instructive to compare the warm H_2 mass to the dust mass in each spectral zone (Table 1). First, we find M(warm H_2)/M(dust) $\sim$80, close to the Galactic value of $\sim$100 in the SF region. Because of the low T_l value in the SF region, there is a large contribution to the H_2 emission from cold gas and we recover almost all of the gas mass. On the other hand, the H_2 emission in the inner disk is dominated by gas with $T > 150$–300 K, and the H_2 line fluxes are insensitive to the presence of colder molecular gas. This is reflected in low values of $M(H_2)/M_{dust} = 1$–4. Colder H_2 may be present, but its emission would be relatively faint and difficult to separate from the emission of the warmest H_2.

4.4. Comparison of H_2 and AGN Energetics

The X-ray luminosity of the nucleus measured by XMM and Chandra, L(2–10 keV) $= 2.0 \times 10^{34}$ W (Bianchi et al. 2009), is not enough to power the observed H_2 luminosity of the inner disk plus nucleus, $L(H_2\ S(0)–S(3)) = 5.7 \times 10^{33}$ W. (The CO 1–0 and CO 2–1 luminosities from the same region are only 3.0×10^{30} W and 2.7×10^{31} W, respectively, and contribute relatively little to cooling the molecular gas.) Following Ogle et al. (2010), the maximum conversion efficiency of X-ray heating, referenced to the 2–10 keV band luminosity, is about
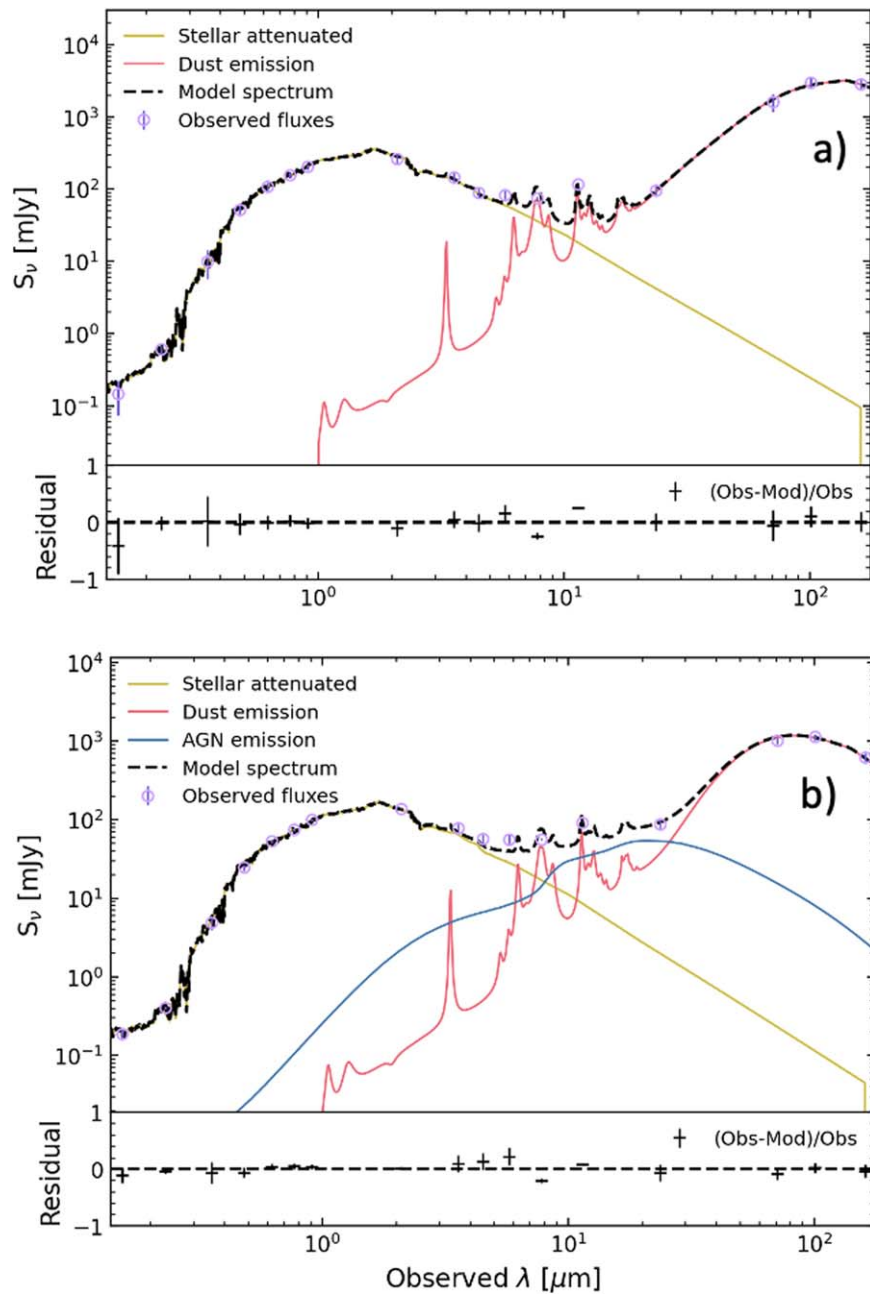
Figure 6. (a) SED of M58 inner disk Zones 1–3, including a dust-attenuated stellar population and emission from dust and PAH molecules. (b) SED fit of the nucleus, including hot dust emission from the AGN.

0.01, whereas the observed ratio is much greater: $L(\mathrm{H_2})/L_\mathrm{X} = L(\mathrm{H_2}\ \mathrm{S(0)–S(3)})/L(2–10\ \mathrm{keV}) = 0.29$. This is similar to 3C radio galaxies (Ogle et al. 2010), where the AGN X-ray luminosity is also not sufficient to power the observed $\mathrm{H_2}$ emission. The relatively low X-ray luminosity of the AGN may also explain why it has no apparent impact on the PAH size distribution. If the X-rays from the AGN are not luminous enough to significantly heat the molecular gas across the kiloparsec-scale inner disk, perhaps they are also ineffective at destroying PAH molecules there. We do not rule out a more significant role for X-ray heating in the unresolved nucleus.

4.5. Molecular Gas and Dust in the Spatially Unresolved AGN

The spiral of dusty warm molecular gas found in the galactic center may be the primary source of fuel powering the AGN.

The Spitzer NUC zone, with $r = 4\farcs6$ (465 pc), contains 33% of the $\mathrm{H_2}$ flux in the inner disk, for both the $\mathrm{H_2}$ 0–0 S(1) and $\mathrm{H_2}$ 1–0 S(1) lines, and 27% of the warm $\mathrm{H_2}$ mass ($3 \times 10^6\ M_\odot$). Our SED fit of the diffuse ISM plus dusty torus in the NUC region yields a cold ISM dust mass of $3 \times 10^5\ M_\odot$, corresponding to a gas mass of $3 \times 10^7\ M_\odot$. The close correspondence between the spatial profiles of the pure rotational and rovibrational lines means that we can reasonably scale the Spitzer NUC values to estimate the warm $\mathrm{H_2}$ mass within the Gemini NIRI PSF. Most of the $\mathrm{H_2}$ 1–0 S(1) flux in the inner disk is resolved by Gemini NIRI (Figure 3), with only 3% contained within $r = 0\farcs35$ (35 pc) of the nucleus. Assuming a constant ratio for $\mathrm{H_2}$ 1–0 S(1)/$\mathrm{H_2}$ 0–0 S(1) yields an unresolved warm $\mathrm{H_2}$ mass of $\sim 9 \times 10^4\ M_\odot$ within this
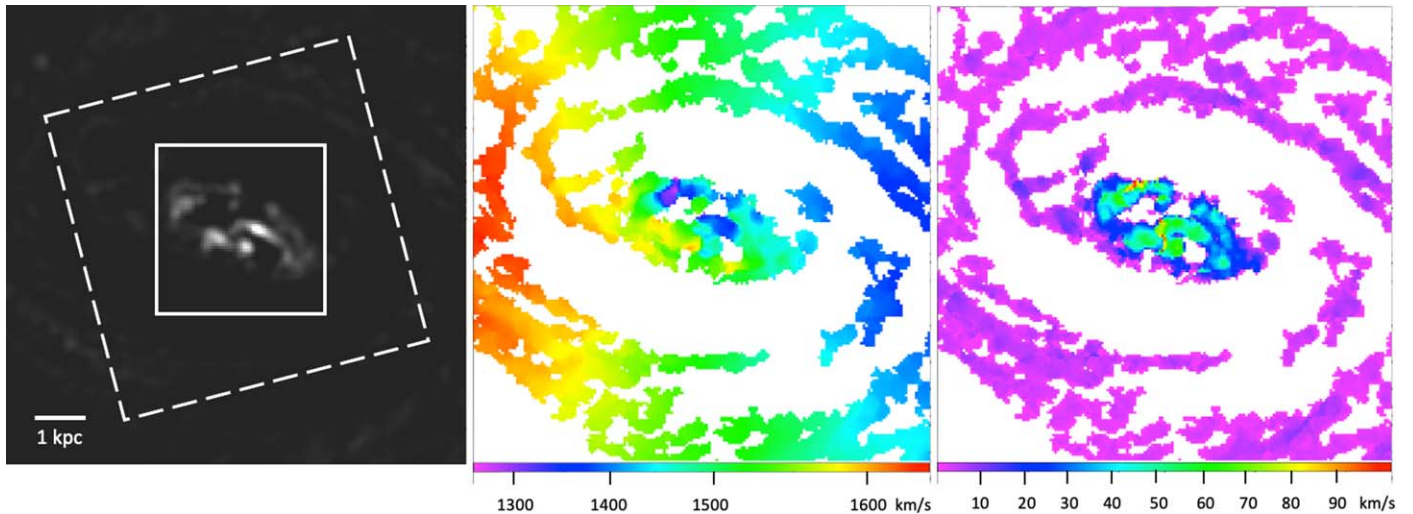
Figure 7. ALMA CO 2–1 emission line moments 0, 1, and 2 from PHANGS-ALMA (Leroy et al. 2021a). The dashed and solid squares correspond to the Spitzer IRS map in Figure 2 and the Gemini H_2 1–0 S(1) image in Figure 3(c). The brightest CO 2–1 emission correlates with high velocity dispersion in Zones 2 and 3 of the inner disk and in the nucleus.

radius. Scaling the dust mass yields a 10 times larger total gas mass of $\sim 9 \times 10^5 \, M_\odot$ within $r = 35$ pc.

As noted above, the nucleus displays pointlike continuum emission at 9–13 μm from silicate dust heated by the AGN. Our model of the NUC SED (Figure 6(b)) employs the SKIRT two-phase dusty torus model (Stalevski 2012; Stalevski et al. 2016). The SED fit does not include the full Spitzer IRS spectrum and therefore does not yield the most accurate torus parameters. For reference, the best-fit torus model from our SED fit has an inclination of $i = 50°$, optical depth $\tau = 3$, and polar dust temperature of 230 K, consistent with the observed silicate emission. Regardless of the large uncertainties in the model, we do obtain a robust torus IR luminosity of $L_{torus} = 3.7 \times 10^{34}$ W that is consistent with the AGN bolometric luminosity of $L_{bol} = 1.0 \times 10^{35}$ W. (Merloni et al. 2003).

We leave a more detailed analysis of the dusty torus spectrum to future work. Together with the existing ALMA CO observations, our upcoming JWST MIRI MRS and NIRSpec IFU observations of the full complement of H_2 pure rotational lines will give the mass, temperature distribution, and kinematics of molecular gas available to fuel the AGN on 10–100 pc scales. They will also map the kinematics and determine mass outflow rates of any ionized or molecular gas outflows, enabling us to determine whether AGN jet feedback is effective at throttling AGN accretion.

4.6. Highly Turbulent CO Kinematics Driven by Jet Feedback

M58 shows evidence of disturbed molecular gas kinematics, as observed in CO 1–0 and 2–1, including components that do not follow the regular rotation curve of the galaxy (Figure 7; García-Burillo et al. 2009; Leroy et al. 2021a; Stuber et al. 2021). We present ALMA CO 2–1 line profiles, extracted from the zones of the inner galaxy where we performed our analysis of the Spitzer spectral maps (Figure 8). Since these lines are integrated over a range of rotational and peculiar velocities, they are broader than the velocity dispersion seen in the spatially resolved map. Relatively narrow line components ($\sigma = 19$–36 km s^{-1}) are found in the SF Zone and Zone 1, following the regular rotation of the galactic disk. Zones 2 and

3 of the inner disk and the nucleus show much broader line components ($\sigma = 60$–120 km s^{-1}). The integrated CO 2–1 line profile of the inner disk plus nucleus shows a single broad peak with $\sigma = 100$ km s^{-1}. Of note is the broad blue wing in Zone 3, which can be seen as anomalously blueshifted emission against the regular rotation of the galactic disk, possibly indicating a molecular outflow component.

The inner disk has a markedly higher velocity dispersion than the surrounding galactic disk (Figure 7). The brightest CO 2–1 emission occurs where the velocity dispersion is $\sigma_{CO} = 40$–60 km s^{-1}, compared to a median of ~ 10 km s^{-1} outside the inner disk. While we do not have direct H_2 kinematic information, we assume it has similar velocity dispersion to the CO 2–1 emitting molecular gas. Under this assumption, we estimate the turbulent kinetic energy of the $3 \times 10^6 \, M_\odot$ of warm H_2 in Zones 2 and 3 to be $\sim 6 \times 10^{45}$ J, for $\sigma_{CO} \sim 50$ km s^{-1}. The corresponding turbulent energy dissipation time for $L(H_2 \, S(0)$–S(3)$) = 3 \times 10^{33}$ W is only 7×10^4 yr. That means that H_2 is a very effective coolant and the turbulent kinetic energy must be replenished with ongoing deposition of kinetic energy by the jet and/or AGN-driven outflows in order to maintain the observed H_2 luminosity.

The high temperature and velocity dispersion of the warm H_2 in the inner disk are not conducive to star formation. At the observed minimum temperature of $T_l \sim 250$ K and density equal to the H_2 0–0 S(3) critical density of $n \sim 10^4$ cm^{-3}, the Jeans mass is $\sim 900 \, M_\odot$. Star formation is unlikely to proceed under these conditions. However, since the warm H_2 percentage is only 1%–4%, it remains to be seen whether star formation may proceed in the cooler, less turbulent cloud cores. The overall lack of star formation in the inner disk suggests that conditions are in fact not conducive to it. However, the presence of a circumnuclear ring of young stars demonstrates that conditions may have been more favorable for star formation at that location in the recent past.

4.7. Jet Shock-ionized Gas with Disturbed Kinematics

We measured ionized gas line fluxes and kinematics from our long-slit optical spectroscopy, extracted along PA = 57° (Figures 9 and 10). We used a BAGPIPES (Carnall et al. 2018)
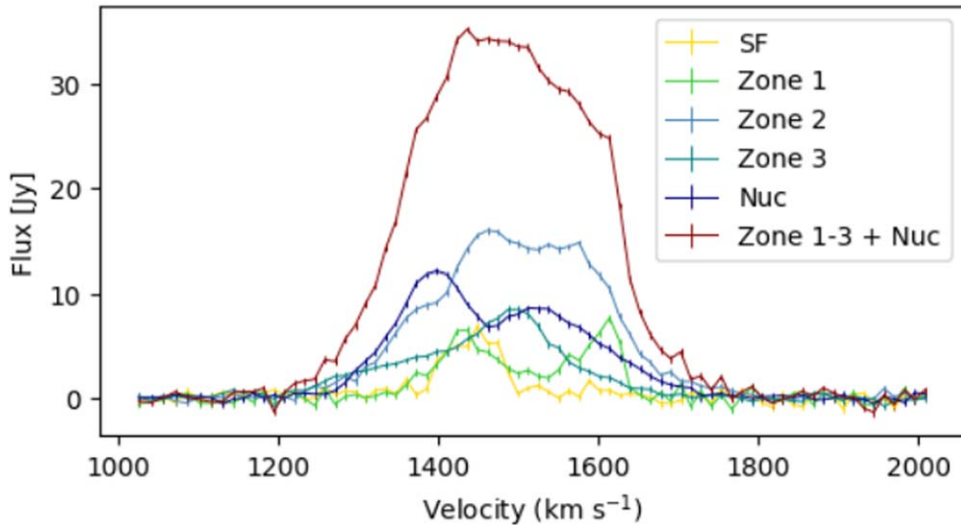
Figure 8. ALMA CO 2–1 emission line profiles for the SF Zone, inner disk Zones 1–3, nucleus, and summed over Zones $1 + 2 + 3 +$ nucleus.
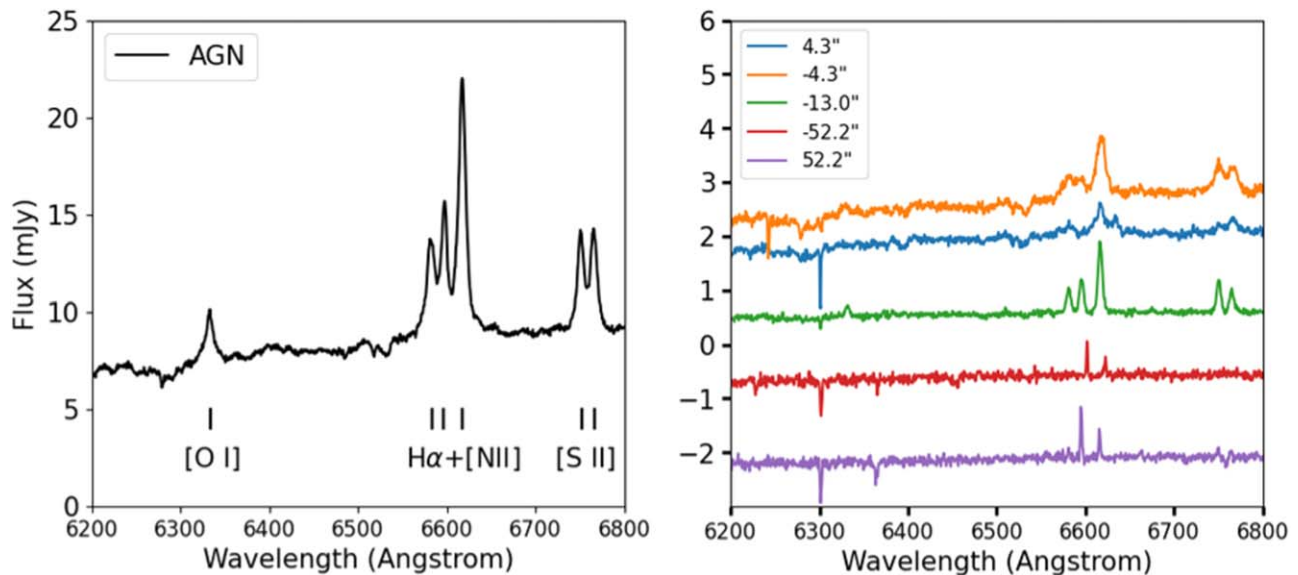

Figure 9. Lick Kast long-slit optical spectra along the major axis of M58. Left: the LINER AGN spectrum, extracted in a $2\farcs2$ wide aperture, displays quite broad forbidden emission lines. Right: spectra labeled by distance from the nucleus. The forbidden emission lines and Hα are very broad within $10''$ (1 kpc) of the AGN, but become narrower at larger distances. The inner disk shows LINER-like line ratios along its entire extent. The emission lines from star-forming regions in spiral arms at 5.3 kpc (offset in flux for clarity) are much narrower and show velocity offsets owing to galaxy rotation.

12 Gyr-old burst model, with exponential decay to model the average stellar population in the inner disk and bulge. A more detailed fit and discussion of the stellar population are outside the scope of this paper. We scaled and subtracted the template from our 2D spectra to remove the stellar continuum, which would otherwise have a large effect on our emission line measurements. We simultaneously fit Gaussian profiles to Hα and the [N II] doublet, tying together the line widths. The [N II] doublet flux ratio was fixed to 1:3 as required by atomic physics, but the [S II] doublet ratio was allowed to vary since it is sensitive to density. We use the center and width of the [N II] 6583.45 Å line to measure velocity and velocity dispersion, and correct the velocity dispersion for the instrumental resolution of $\sigma = 40\,\mathrm{km\,s^{-1}}$.

We find star-forming emission line ratios at the ends of the long slit, where it extends to cover the spiral arms of the galaxy (Figure 9). These star-forming regions follow the overall

rotation of the galaxy. For an assumed disk inclination of $36°$, we find a deprojected rotational speed of $\pm236\,\mathrm{km\,s^{-1}}$ at a distance of $52''$ (5.2 kpc) from the galactic center. The velocity dispersion is low ($<70\,\mathrm{km\,s^{-1}}$), and the lines are marginally resolved or unresolved given the instrumental spectral resolution.

The ionized gas kinematics in the inner disk are highly disturbed (Figure 10), with velocity offsets of -130 to $+300\,\mathrm{km\,s^{-1}}$. The velocity dispersion in this region ranges from 90 to $310\,\mathrm{km\,s^{-1}}$, reaching values considerably higher than the CO velocity dispersion ($\sigma_{\mathrm{CO}} < 120\,\mathrm{km\,s^{-1}}$). The [N II] surface brightness profile declines with increasing radius outside $r = 15''$ (1.5 kpc) and breaks at $r = 23\farcs8$ (2.4 kpc), perhaps delimiting the furthest extent of significant influence of the AGN and radio jet.

At all locations in the inner disk and nucleus of M58, we find [N II]/H$\alpha = 1.5$–2.1, [O I]/H$\alpha = 0.16$–0.38, and [S II]/
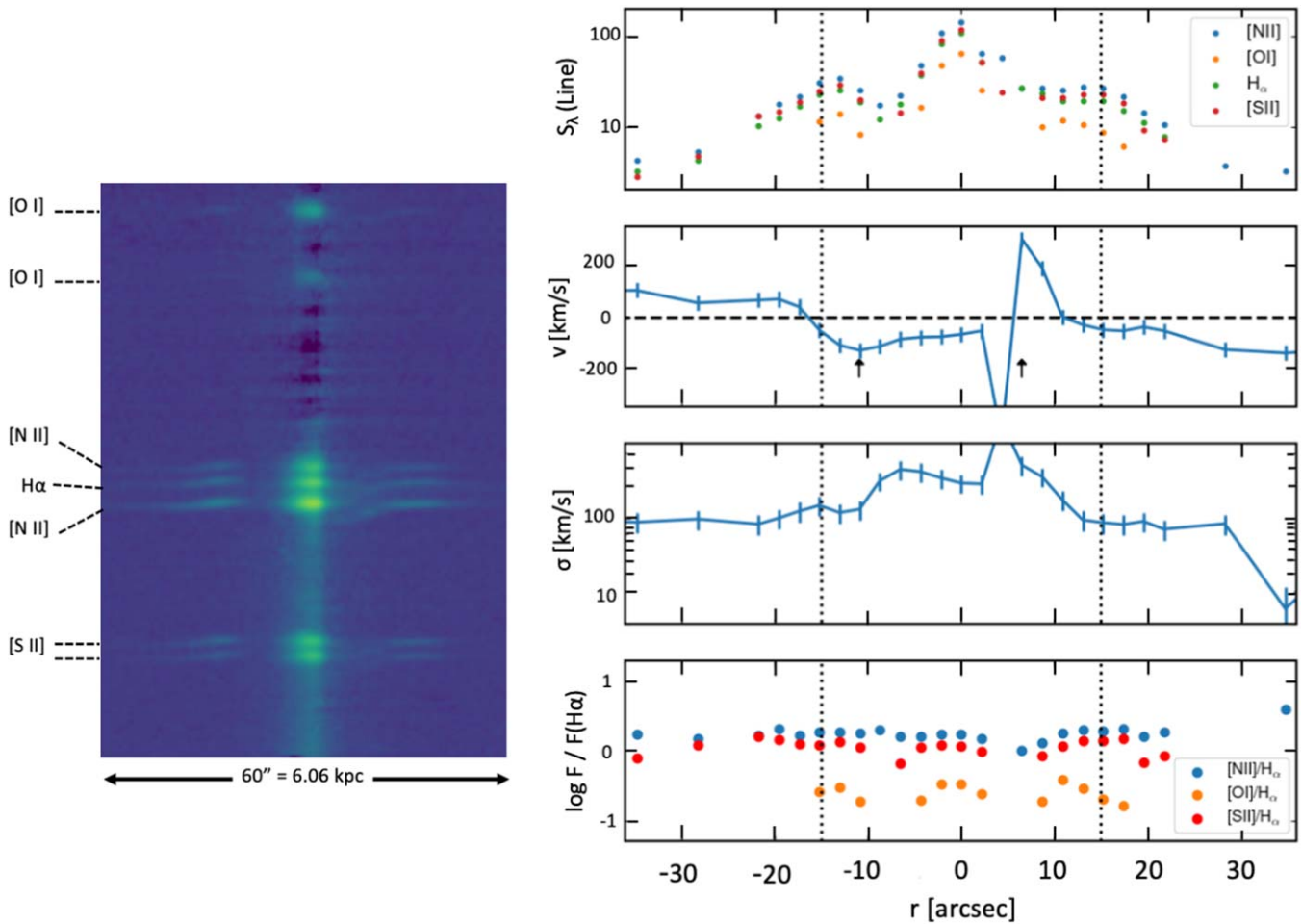
Figure 10. Ionized gas lines in the inner disk. Left: 2D spectrum of [O I] 6300 Å, 6363 Å, Hα + [N II], and the [S II] doublet. The continuum has been subtracted using a stellar population model. The dark horizontal bands are from atmospheric H$_2$O absorption. Note the line splitting 2″–5″ to the right (SSW) of the nucleus. Right: emission line surface brightness [1×10^{-17} W m^{-2} □$^{″-1}$], line of-sight velocity, velocity dispersion, and line flux ratios with respect to Hα. Velocity is corrected for an offset of 146 km s^{-1} from the CO 2–1 systemic velocity of 1480 km s^{-1}. Velocity dispersion is corrected by subtracting the instrumental resolution of 40 km s^{-1} in quadrature. The ionized gas is kinematically disturbed, showing large redshifts and blueshifts relative to the galaxy rotation curve at the arrowed locations. Velocity and velocity dispersion go off-scale at the location of the line splitting, where the fit of a single velocity component is inadequate. Line ratios are consistent with shock heating and/or LINER photoionization.

Hα = 0.7–1.6, characteristic of shocked gas or LINER photoionization. Emission from any star-forming regions in the inner disk is overwhelmed by the extended, high-surface-brightness emission from shocked gas or the AGN. We compare shock models from the MAPPINGS V database (Sutherland & Dopita 2017; Alarie & Morisset 2019), for solar abundance and a characteristic magnetic field strength of 30 μG, to the observed optical line ratios (Figure 11). Taken together, the line ratios are jointly consistent with the models for a narrow range of shock velocities ($V_{sh} = 210$– 260 km s^{-1}). However, a broader range of velocities is allowed ($V_{sh} = 170$–440 km s^{-1}) if each line is emitted under different conditions. This range of shock velocities is broadly consistent with the observed velocities and velocity dispersion of the ionized gas.

We use our JRT image (Figure 3) to measure the Hα + [N II] doublet emission line fluxes in the zones identified in the Spitzer maps (Table 1). The Hα + [N II] line luminosity of the inner disk (Zones 1–3) is 6.3×10^{33} W. Utilizing the optical line ratios observed in our Lick spectrum, we estimate a total optical emission line luminosity of $\sim 9 \times 10^{33}$ W from the inner disk, ~ 1.7 times its H$_2$ pure rotational line luminosity (L(H$_2$

S(0)–S(5)) = 5.4×10^{33} W). Discounting other unmeasured emission lines, this indicates that similar kinetic power is dissipated in the warm molecular and ionized gas phases of the inner disk.

4.8. Prevalence of Jet-shocked Molecular Gas in Nearby Galaxies with Massive Bulges

The presence of strong H$_2$ emission in galaxies with AGNs was clearly demonstrated by Spitzer (Smith et al. 2007b; Roussel et al. 2007; Diamond-Stanic & Rieke 2010; Ogle et al. 2010). We plot H$_2$ 0–0 S(3)/PAH 11.3 against PAH 7.7/11.3 to compare H$_2$ emission from shocks versus star formation (Figure 12). The nuclear spectral types of SINGS galaxies are given by Dale et al. (2006) and Smith et al. (2007b), based on the spectroscopy of Moustakas & Kennicutt (2006). Almost all of the star-forming, non-AGN galaxies in the SINGS sample fall in the lower right corner of this diagram, indicating weak H$_2$ emission and PAH emission dominated by PDRs powered by hot, young stars. Seyfert galaxies, on the other hand, generally have H$_2$/PAH 11.3 > 0.02, indicating shocked molecular gas. Most LINER AGNs have less H$_2$ emission, though several (6/17) do have elevated H$_2$/PAH 11.3,
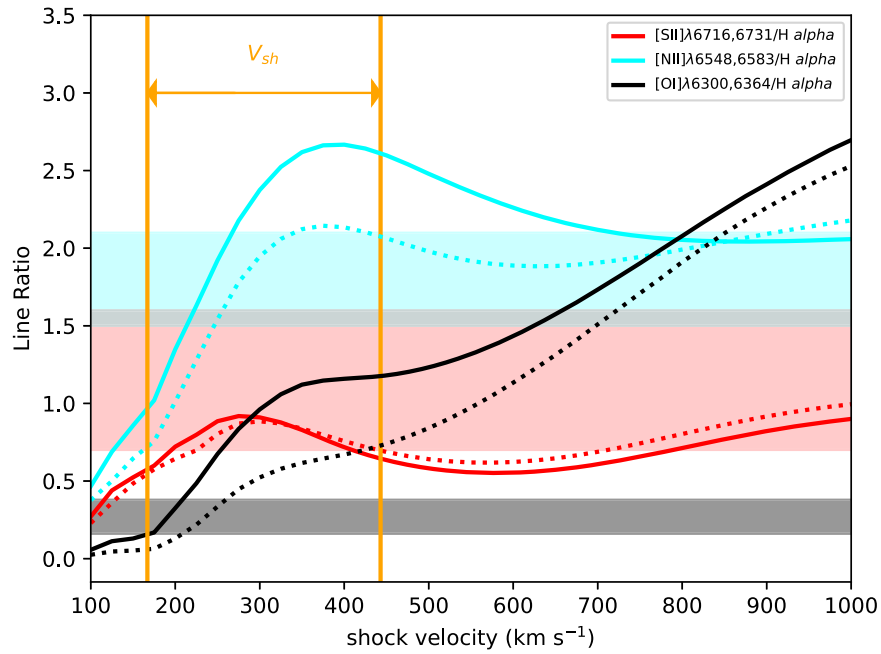
Figure 11. Shock models from the MAPPINGS V database, for solar abundance, 30 μG magnetic field, and two ionized gas densities (solid, dotted: $n = 100, 10$ cm^{-3}). The shaded areas show the observed ranges for three optical line ratios, which individually match the models for shock velocities in the range $V_{sh} = 170$–440 km s^{-1}.
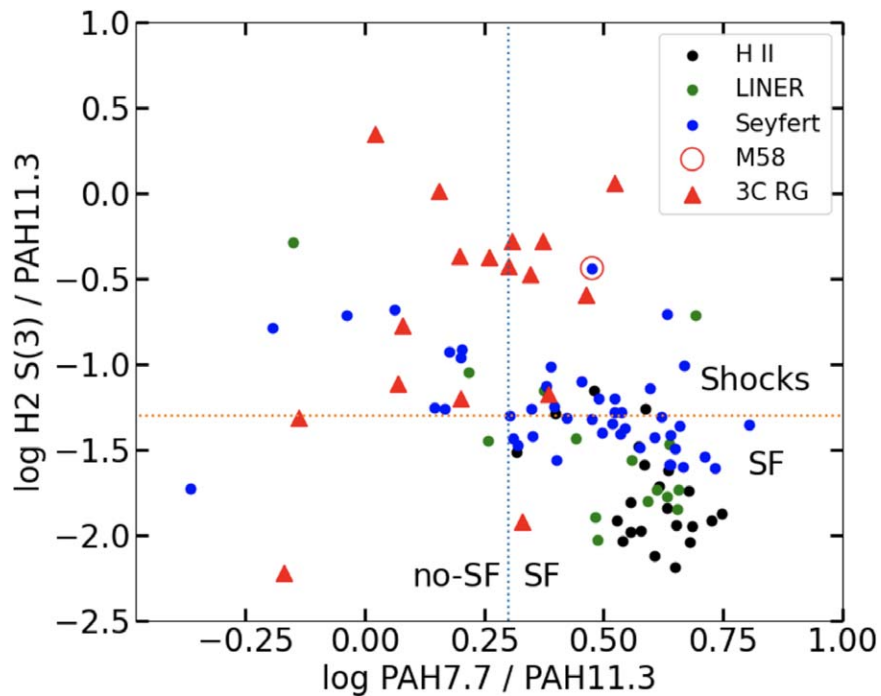
Figure 12. Shocks vs. star formation. Feature flux ratios for galaxy nuclei compiled from the SINGS sample (Smith et al. 2007b; Roussel et al. 2007), supplemented by 35 Seyferts from the revised Shapley-Ames catalog (Diamond-Stanic & Rieke 2010; Sandage & Tamman 1987), and 3C radio galaxies (Ogle et al. 2010). The H$_2$ 0–0 S(3)/PAH 11.3 flux ratio is >0.05 in galaxies with shocked molecular gas. The large value of this ratio in Seyferts and radio galaxies is indicative of AGN kinetic feedback. The PAH 7.7/PAH 11.3 ratio is a good indicator of star formation, falling in the range 2.0–6.0 for most spiral galaxies, and <2.0 for elliptical galaxies. M58 has H$_2$ 0–0 S(3)/PAH 11.3 comparable to the most extreme 3C radio galaxies.

indicating shocked molecular gas. As discussed by Diamond-Stanic & Rieke (2010), for Seyferts, there appears to be an anticorrelation between H$_2$ and PAH 7.7 relative to PAH 11.3, with the strongest H$_2$ emitters having the least PAH 7.7 in their nuclei. They suggest that this may reflect the destruction of small PAHs by shocks. Instead, we suggest that this may be a direct consequence of suppression of star formation in galactic centers by AGN feedback.

M58 has extremely high H$_2$/PAH 11.3 in its inner disk, comparable to the 3C radio galaxies (Ogle et al. 2010). NGC 4258 (not in the SINGS sample) also shows extremely strong H$_2$/PAH 11.3 emission associated with its radio jet (Ogle et al. 2014). In fact, eight of the SINGS galaxies with H$_2$/PAH 11.3 > 0.05 have radio-loud AGNs. Half of these are E/S0 galaxies (NGC 1266, 1316 = Fornax A, 4125, 4552) and the other half are early-type spirals with large bulges (NGC 2841,

4450, M58, 4725). All but one have weak PAH 7.7 μm emission in their Spitzer spectra, indicating little star formation in the galactic center. The one exception is the peculiar, post-starburst galaxy NGC 1266, which may have ongoing nuclear star formation and is well known for its jet-driven molecular outflow (Alatalo et al. 2014). All of these galaxies have massive bulges and supermassive black holes capable of launching radio jets. The association of excess H_2 emission with radio-loud AGNs supports the hypothesis that the warm molecular gas in these galaxies is heated by radio jet feedback. The lack of star formation in the centers of these galaxies is also consistent with the hypothesis that this feedback mechanism suppresses star formation.

4.9. Multiphase Jet–Disk Interaction

Our Spitzer IRS and Gemini observations of the inner disk of M58 reveal copious emission in pure rotational and rovibrational lines of warm H_2. As we have shown, this emission is too luminous to be powered by X-rays from the AGN. Similar power is emitted in optical emission lines from ionized gas in the region, with line ratios indicative of shock heating. Both molecular and ionized gas have large velocity dispersion, providing a reservoir of kinetic energy and turbulence that may be the proximate power source for the high-surface-brightness line emission. M58 is one of eight radio-loud AGNs in the SINGS sample that display luminous H_2 emission and H_2/PAH $11.3 > 0.05$, supporting the idea that the radio jet may be the primary power source in the kiloparsec-scale disk. Extended X-ray emission is also found in the inner disk of M58, perhaps tracing the edges of the hot radio jet cocoon, where it intersects dense gas associated with the spiral molecular gas lanes (Figure 1(b)).

We suggest that the rich phenomenology described above can be explained by the interaction of the M58 radio jet cocoon with the ISM of the inner disk. Unlike the anomalous arms in NGC 4258 (Ogle et al. 2014), where the radio jet is initially directed in the plane of the disk, the morphology of the shocked molecular and ionized gas emission in M58 is consistent with a radio jet oriented perpendicular to the disk. The radio jet drives an energy bubble into the ISM, which intersects the inner disk in a roughly circular footprint. The spiral structure inside this footprint comes from dusty molecular gas organized in a spiral lane that converges on the nucleus of the galaxy. The waist of the radio jet cocoon, as delimited by the region of highest CO velocity dispersion and surface brightness, is currently restricted to a radius of 1.6 kpc. Lower-surface-brightness emission from H_2 and ionized gas out to 2.6 kpc (in Zone 1) may be energized by residual turbulence in gas that has been disturbed by prior radio outbursts that have expanded outward to this larger radius.

We estimate the M58 jet power to be $P_{jet} \sim 2 \times 10^{36}$ W from its 1.4 GHz radio power of $\nu S_\nu = 1.4 \times 10^{32}$ W, using the relation of Cavagnolo et al. (2010), which is based on the measurement of jet cavity powers for low-power radio jets. The power we measure in the H_2 S(0)–S(3) pure rotational and optical ionized gas lines amounts to $\sim$0.2% and 0.5%, respectively, of this estimate of jet power. The jet power is therefore much more than sufficient to drive the observed line emission from the inner disk. Only a very small percentage of the jet power is deposited into the inner disk, since the jet has escaped the confines of the disk, extending at least 7 kpc into the galaxy halo.

The energy of the hot radio jet cocoon may be transferred directly to the molecular gas by shocks driven into the spiral lanes by the cocoon, or by a higher-density wind of ionized gas that blows outward from the nucleus. Similar phenomenology is seen in planetary nebulae, where a hot, ionized wind ablates knots of molecular gas, forming cometary tails of molecular gas that emit strongly in H_2. The high systematic velocity offsets of ionized gas that we observe may be consistent with ionized outflow. Further, more detailed spectral mapping of ionized gas in the inner disk is needed to confirm this.

Our description of the radio-jet AGN feedback in M58 is both motivated and supported by hydrodynamical simulations of the propagation of radio jets through a clumpy, multiphase ISM (Mukherjee et al. 2016, 2018; Meenakshi et al. 2022). The jet–disk simulations (Mukherjee et al. 2018) only employ powerful jets ($P_{jet} = 10^{38}$–10^{39} W), typical of radio galaxies, so a quantitative comparison of our results with these simulations is not possible. Instead, we compare our results to the simulations of lower-power jets ($P_{jet} = 10^{36}$–10^{38} W), comparable to the M58 jet, propagating in an initially spherical ISM geometry (Mukherjee et al. 2016). These simulations show that the radio jet creates a hot energy bubble in the ISM, surrounded by a forward shock. Dense clouds are shredded and accelerated in the hot energy bubble, creating a wind. Low-power jets like the M58 jet are trapped for a longer time than high-power jets, potentially hollowing out a large cavity in the ISM. However, low-power jets are less effective than high-power jets at accelerating clouds to high velocities, with outflows attaining velocities of <300 km s^{-1}, comparable to the ionized gas velocities we observe in M58. The simulations do not include a molecular gas component, so there is no direct prediction of the effects of the jet on the H_2 temperature and velocity dispersion.

5. Summary and Conclusions

We find high-surface-brightness H_2 and CO emission from warm molecular gas in the inner ($r = 2.6$ kpc) disk of the spiral galaxy M58. This corresponds to emission of similar brightness from ionized gas lines and thermal X-ray emission. The optical forbidden line ratios from ionized gas in the inner disk are consistent with shock heating by low-velocity shocks ($V_{sh} = 170$–440 km s^{-1}). We suggest that the molecular and ionized gas emissions are excited by shocks and turbulence driven by the radio jet cocoon and radio-jet-driven outflows into the multiphase ISM. The observed high velocity dispersion of the molecular and ionized gas allows it to serve as a reservoir of kinetic energy that must be constantly replenished in order to support the observed H_2 and ionized gas line luminosity.

The PAH mass fraction and feature ratios in the inner disk of M58 indicate normal PAH abundances for gas of solar metallicity, with no significant contribution from star-forming regions. The PAH emission is likely excited by the diffuse radiation field from old stars in the bulge of M58. There is no indication of PAH destruction by jet-driven shocks or X-rays from the AGN.

Eight other massive, nearby galaxies observed by Spitzer show high H_2 0–0 S(3)/PAH 11.3 (>0.05), similar to M58 and the 3C radio galaxies. All of these H_2-luminous galaxies have radio-loud AGNs. This supports a picture where radio jet feedback is very disruptive to gas in galactic centers, driving shocks and turbulence that heat both the ionized and molecular ISM. The high molecular gas temperatures and turbulence in the inner disk of M58 most certainly are not conducive to star

formation, and may be a signature of negative radio jet feedback on star formation. On the other hand, most Seyfert galaxies show lower levels of enhanced H_2 emission, possibly excited by less powerful radio-quiet AGN outflows. The observed anticorrelation between H_2 and PAH 7.7 μm emission in Seyferts indicates that star formation may also be suppressed by radio-quiet AGNs.

ORCID iDs

Patrick M. Ogle ⓘ https://orcid.org/0000-0002-3471-981X
Iván E. López ⓘ https://orcid.org/0000-0003-4687-8401
Victoria Reynaldi ⓘ https://orcid.org/0000-0002-6472-6711
Aditya Togi ⓘ https://orcid.org/0000-0001-5042-3421
R. Michael Rich ⓘ https://orcid.org/0000-0003-0427-8387
Javier Román ⓘ https://orcid.org/0000-0002-3849-3467
Zhuofu (Chester) Li ⓘ https://orcid.org/0000-0003-4285-4453
Grant Donnelly ⓘ https://orcid.org/0009-0001-6065-0414
J. D. T. Smith ⓘ https://orcid.org/0000-0003-1545-5078
Philip N. Appleton ⓘ https://orcid.org/0000-0002-7607-8766
Lauranne Lanz ⓘ https://orcid.org/0000-0002-3249-8224

References

Aird, J., Coil, A. L., Georgakakis, A., et al. 2015, MNRAS, 451, 1892
Akhlaghi, M., & Ichikawa, T. 2015, ApJS, 220, 1
Alarie, A., & Morisset, C. 2019, RMxAA, 55, 377
Alatalo, K., Nyland, K., Graves, G., et al. 2014, ApJ, 780, 186
Appleton, P. N., Diaz-Santos, T., Fadda, D., et al. 2018, ApJ, 869, 61
Astropy Collaboration, Price-Whelan, A. M., Lim, P. L., et al. 2022, ApJ, 935, 167
Barth, A. J., Ho, L. C., Filippenko, A. V., Rix, H.-W., & Sargent, W. L. W. 2001, ApJ, 546, 205
Bertin, E. 2006, in ASP Conf. Ser. 351, Astronomical Data Analysis Software and Systems XV, ed. C. Gabriel et al. (San Francisco, CA: ASP), 112
Bertin, E., & Arnouts, S. 1996, A&AS, 117, 393
Bianchi, S., Guainazzi, M., Matt, G., Fonseca Bonilla, N., & Ponti, G. 2009, A&A, 495, 421
Boogaard, L. A., Decarli, R., Walter, F., et al. 2023, ApJ, 945, 111
Boquien, M., Burgarella, D., Roehlly, Y., et al. 2019, A&A, 622, A103
Carnall, A. C., McLure, R. J., Dunlop, J. S., & Davé, R. 2018, MNRAS, 480, 4379
Cavagnolo, K. W., McNamara, B. R., Nulsen, P. E. J., et al. 2010, ApJ, 720, 1066
Chastenet, J., Sutter, J., Sandstrom, K., et al. 2023, ApJL, 944, L12
Chiaraluce, E., Bruni, G., Panessa, F., et al. 2019, MNRAS, 485, 3185
Comerón, S., Knapen, J. H., Beckman, J. E., & Shlosman, I. 2008, A&A, 478, 403
Croton, D. J., Springel, V., White, S. D. M., et al. 2006, MNRAS, 365, 11
Dale, D. A., Smith, J. D. T., Armus, L., et al. 2006, ApJ, 646, 161
de los Reyes, M. A. C., & Kennicutt, R. C. J. 2019a, ApJ, 872, 16
de los Reyes, M. A. C., & Kennicutt, R. C. J. 2019b, ApJ, 878, 74
Developers, J., Averbukh, J., Bradley, L., et al. 2023, Jdaviz, v3.7.1, Zenodo, doi:10.5281/zenodo.5513927
Diamond-Stanic, A. M., & Rieke, G. H. 2010, ApJ, 724, 140
Draine, B. T., Aniano, G., Krause, O., et al. 2014, ApJ, 780, 172
Draine, B. T., & Li, A. 2007, ApJ, 657, 810
Draine, B. T., Li, A., Hensley, B. S., et al. 2021, ApJ, 917, 3
Eracleous, M., Shields, J. C., Chartas, G., & Moran, E. C. 2002, ApJ, 565, 108
García-Bernete, I., Rigopoulou, D., Alonso-Herrero, A., et al. 2022, MNRAS, 509, 4256

García-Burillo, S., Fernández-García, S., Combes, F., et al. 2009, A&A, 496, 85

Gensior, J., Kruijssen, J. M. D., & Keller, B. W. 2020, MNRAS, 495, 199

Groves, B., Krause, O., Sandstrom, K., et al. 2012, MNRAS, 426, 892

Harrison, C. M., Thomson, A. P., Alexander, D. M., et al. 2015, ApJ, 800, 45

Higdon, S. J. U., Armus, L., Higdon, J. L., Soifer, B. T., & Spoon, H. W. W. 2006, ApJ, 648, 323

Ho, L. C., & Ulvestad, J. S. 2001, ApJS, 133, 77

Hopkins, P. F., Somerville, R. S., Hernquist, L., et al. 2006, ApJ, 652, 864

Kaneda, H., Onaka, T., Sakon, I., et al. 2008, ApJ, 684, 270

Kennicutt, R. C. J., Armus, L., & Bendo, G. 2003, PASP, 115, 928

Kormendy, J., & Ho, L. C. 2013, ARA&A, 51, 511

Labrie, K., Anderson, K., Cárdenes, R., Simpson, C., & Turner, J. E. H. 2019, in ASP Conf. Ser. 523, Astronomical Data Analysis Software and Systems XXVII, ed. P. J. Teuben et al. (San Francisco, CA: ASP), 321

Lambrides, E. L., Petric, A. O., Tchernyshyov, K., Zakamska, N. L., & Watts, D. J. 2019, MNRAS, 487, 1823

Lang, D., Hogg, D. W., Mierle, K., Blanton, M., & Roweis, S. 2010, AJ, 139, 1782

Leroy, A. K., Schinnerer, E., Hughes, A., et al. 2021a, ApJS, 257, 43

Leroy, A. K., Hughes, A., Liu, D., et al. 2021b, ApJS, 255, 19

Madau, P., & Dickinson, M. 2014, ARA&A, 52, 415

Maiolino, R., Ruiz, M., Rieke, G. H., & Papadopoulos, P. 1997, ApJ, 485, 552

Martig, M., Bournaud, F., Teyssier, R., & Dekel, A. 2009, ApJ, 707, 250

Meenakshi, M., Mukherjee, D., Wagner, A. Y., et al. 2022, MNRAS, 516, 766

Merloni, A., Heinz, S., & di Matteo, T. 2003, MNRAS, 345, 1057

Moustakas, J., & Kennicutt, R. C. J. 2006, ApJS, 164, 81

Mukherjee, D., Bicknell, G. V., Sutherland, R., & Wagner, A. 2016, MNRAS, 461, 967

Mukherjee, D., Bicknell, G. V., Wagner, A. Y., Sutherland, R. S., & Silk, J. 2018, MNRAS, 479, 5544

Nagar, N. M., Falcke, H., & Wilson, A. S. 2005, A&A, 435, 521

Nemmen, R. S., Storchi-Bergmann, T., & Eracleous, M. 2014, MNRAS, 438, 2804

Nersesian, A., Xilouris, E. M., Bianchi, S., et al. 2019, A&A, 624, A80

Newville, M., Otten, R., Nelson, A., et al. 2023, lmfit/lmfit-py: v1.2.2, Zenodo, doi:10.5281/zenodo.8145703

Ogle, P., Boulanger, F., Guillard, P., et al. 2010, ApJ, 724, 1193

Ogle, P. M., Lanz, L., & Appleton, P. N. 2014, ApJL, 788, L33

Pilbratt, G. L., Riedinger, J. R., Passvogel, T., et al. 2010, A&A, 518, L1

Pogge, R. W. 1989, ApJS, 71, 433

Poglitsch, A., Waelkens, C., Geis, N., et al. 2010, A&A, 518, L2

Rich, R. M., Mosenkov, A., Lee-Saunders, H., et al. 2019, MNRAS, 490, 1539

Roussel, H., Helou, G., Hollenbach, D. J., et al. 2007, ApJ, 669, 959

Roussel, H., Sauvage, M., Vigroux, L., & Bosma, A. 2001, A&A, 372, 427

Ruiz-Lapuente, P. 1996, ApJL, 465, L83

Smith, J. D. T., Armus, L., Dale, D. A., et al. 2007a, PASP, 119, 1133

Sandage, A., & Tamman, G. A. 1987, A Revised Shapley-Ames Catalog of Bright Galaxies (2nd ed.; Washington, DC: Carnegie Institution)

Smith, J. D. T., Draine, B. T., Dale, D. A., et al. 2007b, ApJ, 656, 770

Springel, V., Di Matteo, T., & Hernquist, L. 2005, ApJL, 620, L79

Stalevski, M. 2012, BlgAJ, 18, 3

Stalevski, M., Ricci, C., Ueda, Y., et al. 2016, MNRAS, 458, 2288

Stuber, S. K., Saito, T., Schinnerer, E., et al. 2021, A&A, 653, A172

Sutherland, R. S., & Dopita, M. A. 2017, ApJS, 229, 34

Theios, R. L., Malkan, M. A., & Ross, N. R. 2016, ApJ, 822, 45

Togi, A., & Smith, J. D. T. 2016, ApJ, 830, 18

van der Kruit, P. C., Oort, J. H., & Mathewson, D. S. 1972, A&A, 21, 169

Veilleux, S., Rupke, D. S. N., & Swaters, R. 2009, ApJL, 700, L149

Vollmer, B., Soida, M., Beck, R., et al. 2013, A&A, 553, A116

Yang, G., Boquien, M., Buat, V., et al. 2020, MNRAS, 491, 740

Yang, G., Brandt, W. N., Vito, F., et al. 2018, MNRAS, 475, 1887

Zhang, L., Ho, L. C., & Li, A. 2022, ApJ, 939, 22